Computers and Geosciences 109 (2017) 1–15

Contents lists available at ScienceDirect

Computers and Geosciences

journal homepage: www.elsevier.com/locate/cageo

Research paper

Iterative refinement of implicit boundary models for improved geological feature reproduction

Ryan Martin [a,b,*], Jeff B. Boisvert [a,b]

[a] Center for Computational Geostatistics, Edmonton, Canada
[b] University of Alberta, Edmonton, Canada

ARTICLE INFO

Keywords:
Geological modeling
Non-stationarity
Radial basis functions
Partition of unity
Geostatistics

ABSTRACT

Geological domains contain non-stationary features that cannot be described by a single direction of continuity. Non-stationary estimation frameworks generate more realistic curvilinear interpretations of subsurface geometries. A radial basis function (RBF) based implicit modeling framework using domain decomposition is developed that permits introduction of locally varying orientations and magnitudes of anisotropy for boundary models to better account for the local variability of complex geological deposits. The interpolation framework is paired with a method to automatically infer the locally predominant orientations, which results in a rapid and robust iterative non-stationary boundary modeling technique that can refine locally anisotropic geological shapes automatically from the sample data. The method also permits quantification of the volumetric uncertainty associated with the boundary modeling. The methodology is demonstrated on a porphyry dataset and shows improved local geological features.

1. Introduction

The purpose of boundary modeling is to generate contiguous geological domains inside which mineral resources and reserves will be estimated. Boundary modeling is the workflow that assigns the geological interpretation embedded in a set of categorical variables to the unsampled locations in a domain; this ensures an estimate made at an unsampled location uses the corresponding related samples. Boundaries are traditionally modeled using explicit methods; where the orientation and extent of the different geological bodies are interpreted on a set of 2D cross sections and the individual interpretations are stitched together to form 3D geological shapes. Recently implicit methods are applied to this problem. Implicit boundary modeling is the automatic extraction of geological surface from a scalar function sampled at the data locations. The signed distance function (SDF) is the most common scalar function for geological applications and is computed from the locations of the categorical data. The SDF is the shortest distance from each sample location to another sample location of a different category (Wilde and Deutsch, 2012). In this work the SDF is negative if the current location is of the category of interest and positive if the current location is something different; the specific choice of sign is arbitrary. The SDF is first interpolated at the data locations, then evaluated on a set of grid locations spanning the domain, and finally the boundary is extracted by finding the location of the 0-level surface, for example with marching cubes (Lorensen and Cline, 1987). Implicit modeling methods have beneficial properties such as auditability, rapid model construction and easy updating, and are widely applied to geological modeling problems.

Any interpolation method can be used to evaluate the SDF at the unsampled locations, including: kriging; inverse distance weighted (IDW); or radial basis function (RBF) interpolators. The RBF interpolator is popular in the geological modeling literature (Cowan et al., 2003; Hillier et al., 2014; Knight et al., 2007; Vollgger et al., 2015) and is identical to the dual kriging interpolator given the choice of covariance function and radial kernel (Fazio and Roisenberg, 2013; Journel, 1989). These interpolators make an assumption of second order stationarity, that is, the spatial relationships between locations are constant throughout the domain. For example, dual kriging assumes a constant covariance function modeled by calculating and fitting the experimental variogram, whereas RBFs rely on a kernel parameterized for the data configuration in the given domain (Fasshauer, 2007). Anisotropy is often present in geological domains but a set of anisotropic parameters applied globally may not adequately describe structurally complex domains. Manual data-partitioning and unfolding techniques can be applied to account for many cases of local anisotropy and second-order non-stationary kriging frameworks are available for more complicated domains (Boisvert and Deutsch, 2011; Machuca-Mory and Deutsch, 2013).

* Corresponding author. Donadeo Innovation Centre for Engineering, 9211-116 Street, University of Alberta, Edmonton, Alberta T6G 1H9,
E-mail addresses: rdm1@ualberta.ca (R. Martin), jbb@ualberta.ca (J.B. Boisvert).

http://dx.doi.org/10.1016/j.cageo.2017.07.003
Received 5 December 2016; Received in revised form 17 May 2017; Accepted 13 July 2017
Available online 21 July 2017

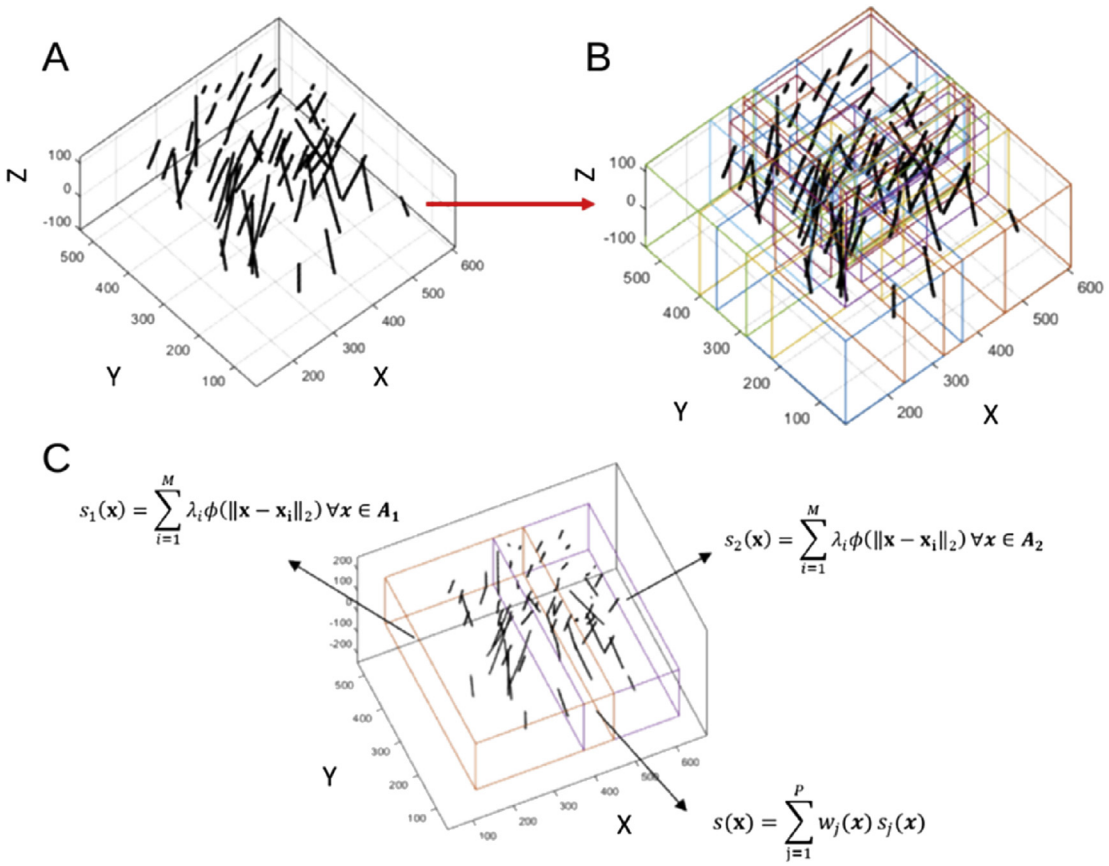

Fig. 1. Schematic example of the binary partitioning algorithm. A) the domain with scattered drill holes and the corresponding extents of the mesh, B) final set of partitions generated from binary decomposition, C) local interpolants are solved independently in each partition, on overlapping sites the local interpolants $s_j(\boldsymbol{x})$ are weighted to the global interpolant $s(\boldsymbol{x})$.

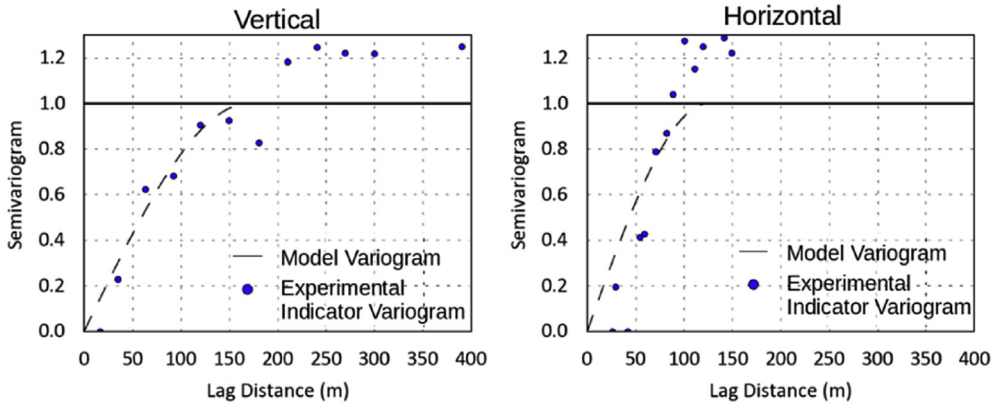

Fig. 2. Standardized experimental and model indicator variograms for category 2 in the vertical direction (left) and horizontal direction (right). Data is fit with a single structure spherical model to permit a positive definite covariance function.

However, frameworks for local orientations in RBF interpolation are mainly developed for the case of sparse geological information, where the dataset for implicit reconstruction includes orientation measurements of the target geological surfaces (Hillier et al., 2014). In these instances, locally curvilinear features in boundary models are improved by incorporating the either on-contact or off-contact orientations that inform the geometry of the target surface (Hillier et al., 2014; Lajaunie et al., 1997). The framework developed by Hillier et al. (2014) allows for the incorporation of several types of constraints that can control the orientation of the boundary locally but this framework requires structural measurements to inform the surface orientations.

The proposed methodology is a non-stationary boundary interpolation method for the case where there are abundant data and local anisotropic properties can be inferred directly from the samples. This is common in the mining case where abundant data are available to construct the models and advanced visualization techniques (such as the "X-Ray Plunge"; Cowan, 2014) are required to correctly model the complex orientations of continuity in 3D. In these types of domains, implicit models that account for local continuities better capture geological relationships. A semi-automatic iterative framework is proposed where the local orientations of continuity are inferred from the generated geomodels and the iteratively refined boundaries better reflect the target geological shapes.

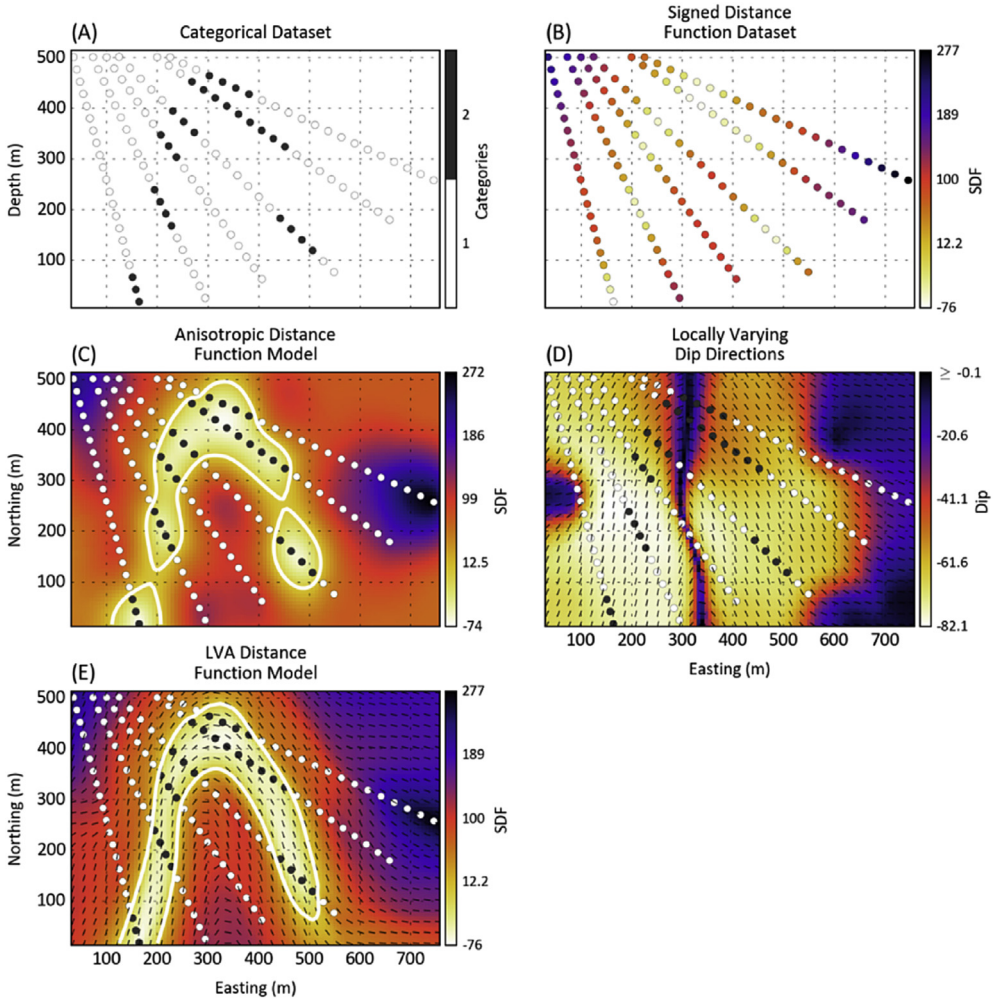

Fig. 3. SDF Modeling workflow to account for curvilinear geological features. A) categorical dataset, B) signed distance function values calculated from the indicator dataset, C) the distance function model generated with the variogram models shown in Fig. 2, D) LVA-field dip component extracted from the anisotropic model in C, and E) the refined locally anisotropic boundary model generated with LVA kriging.

1.1. Background

The following is summarized from Fasshauer (2007). Radial basis functions fit a function to a scalar field that is sampled at a set of scattered data locations. For geological modeling the scalar function is often the SDF calculated from the locations of indicator data. Consider a set of scattered data locations in R^3 represented by $\mathbf{x}_i = (x, y, z)$ where the value of the SDF, $f(\mathbf{x}_i)$, is calculated for all $i = 1, \ldots, \mathrm{M}$ data sites. The goal of RBF interpolation is to obtain a function that interpolates $f(\mathbf{x}_i)$ for all $\mathbf{x}_i$ in the domain. The interpolant $s(\mathbf{x})$ is a grid-free continuous function defined for all locations $\mathbf{x}$. The value of the interpolant at any location $\mathbf{x}$ is obtained from the weighted linear combination of all data evaluated on a radial kernel, ϕ:

$$s(\mathbf{x}) = \sum_{i=1}^{M} \lambda_i \phi(\|\mathbf{x} - \mathbf{x_i}\|_2) \tag{1}$$

where λ is the vector of weights solved under the constraint that the interpolant, $s(\boldsymbol{x_i})$, interpolates the scalar function at the data locations, $f(\boldsymbol{x_i})$, e.g.:

$$s(\mathbf{x}_i) = f(\mathbf{x}_i) \quad i = 1, \ldots, \mathrm{M}$$

The problem formulated in this way leads to a linear system of equations:

$$\boldsymbol{A\lambda} = \boldsymbol{f}$$

where the square interpolation matrix $\boldsymbol{A}$ has components $A_{ij} = \phi(\|\mathbf{x}_i - \mathbf{x}_j\|_2)$ for $i, j = 1, \ldots, \mathrm{M}$, $\boldsymbol{f}$ is a column vector containing the value of the SDF, $f(\mathbf{x}_i)$, at location $\mathbf{x}_i$ for $i = 1, \ldots, \mathrm{M}$, and λ is a column vector of weights that are determined by solving the linear system of equations. Once the weights are determined, the value of the interpolant can be extracted for any location (Equation (1)). The kernel type, anisotropy and interpolation parameters are problem specific and depend on the data configuration and desired surface properties. The kernel determines the spatial relationship between all $i - j$ points evaluated with the Euclidean distance. Global anisotropy can be introduced using an anisotropic kernel (Hillier et al., 2014).

Historically the main issue for applying RBF-interpolation to large geological datasets is the dense linear system of equations and the resulting issues with CPU and RAM requirements (Beatson et al., 1999; Carr et al., 2001; Cowan et al., 2003). There are many methods to permit RBF interpolation for large datasets: sparse-direct interpolation where the influence of points beyond some distance from one another is negligible (Ohtake et al., 2006); iterative solving techniques that assume a sparse system of equations and some level of accuracy (Beatson et al., 1999; Carr et al., 2001); and domain decomposition techniques which partition the domain into overlapping subsets and solve many small sub-problems, often in parallel (Beatson et al., 2001; Cuomo et al., 2013;

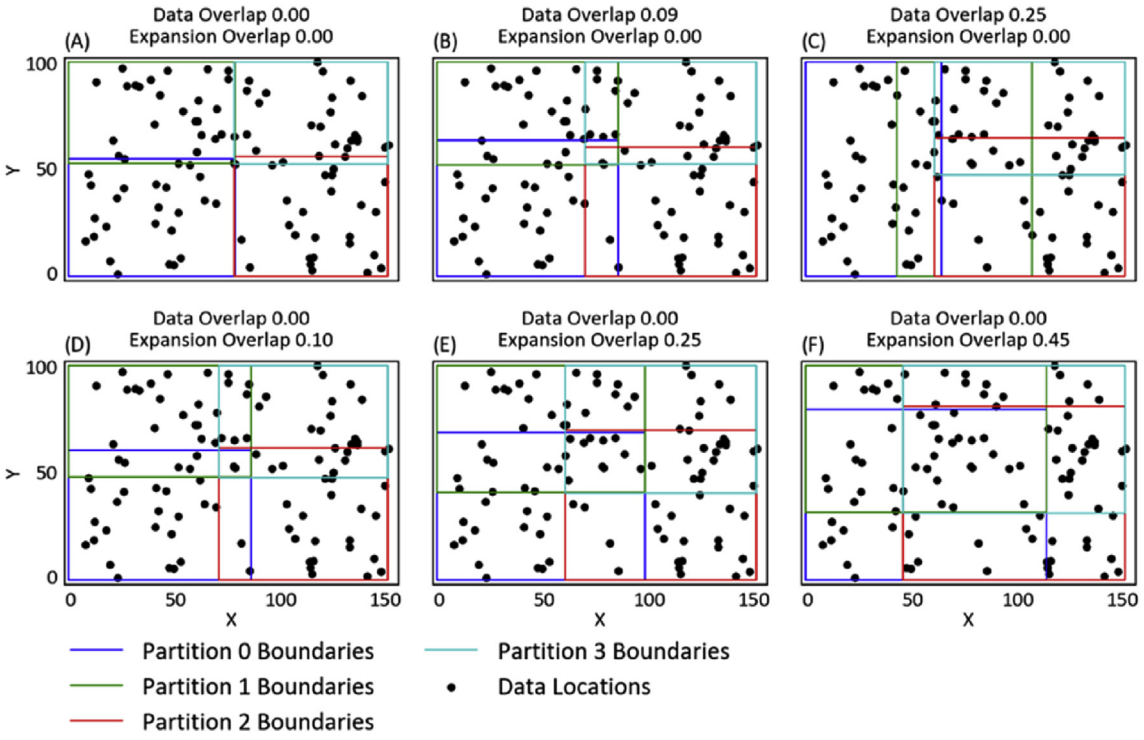

Fig. 4. Examples of the overlap obtained during binary partitioning. A-C) partition overlap generated by considering data overlap in child partitions during splitting, D-F) partition overlap generated by considering expansion of the partitions after decomposition.

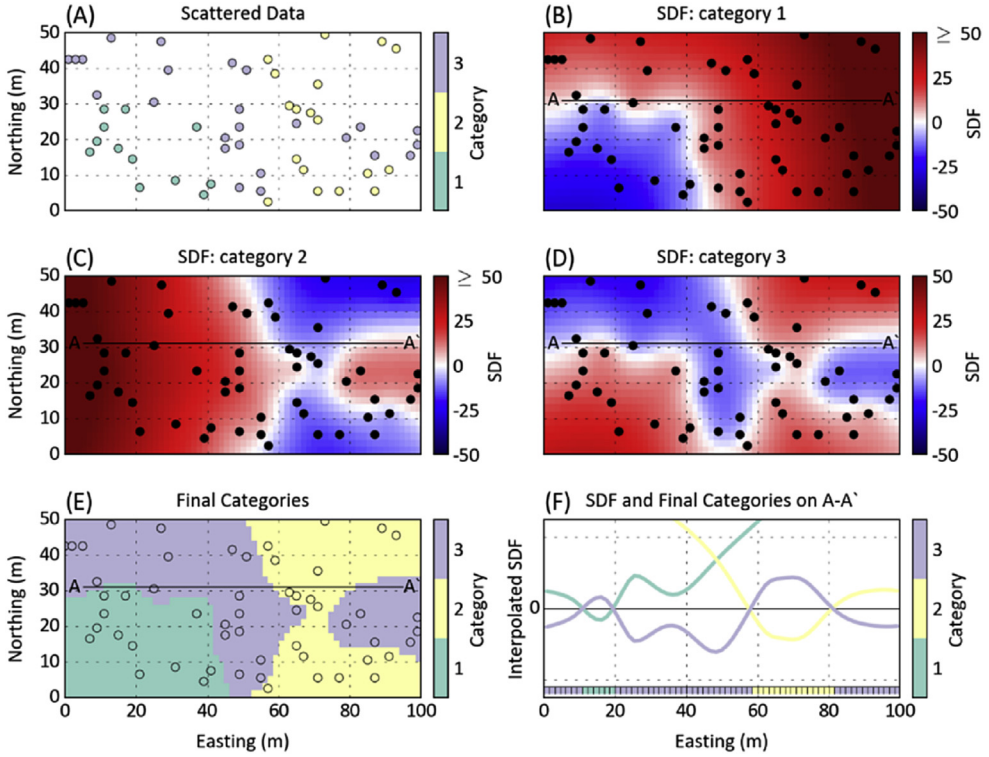

Fig. 5. Example of the N-category extraction from the independent N-SDF interpolations (Silva, 2015). A) the simple example domain of 3 categories. B-D) SDF interpolants for categories 1, 2 and 3, respectively. E) the final categories prevailing at each location in the grid given the interpolated SDF values for each category.

Ohtake et al., 2003; Pouderoux et al., 2004; Xiaojun et al., 2005).

The Partition of Unity (PU) domain decomposition recursively decomposes a domain, A, into P overlapping subdomains, A_j, so that $\cup_{j=1}^{P} A_j = A$ (Fig. 1a and b)). In each partition a local interpolant is obtained considering the contained data, and the global interpolant, $s(\boldsymbol{x})$, is reconstructed from the linear combination of the local interpolants

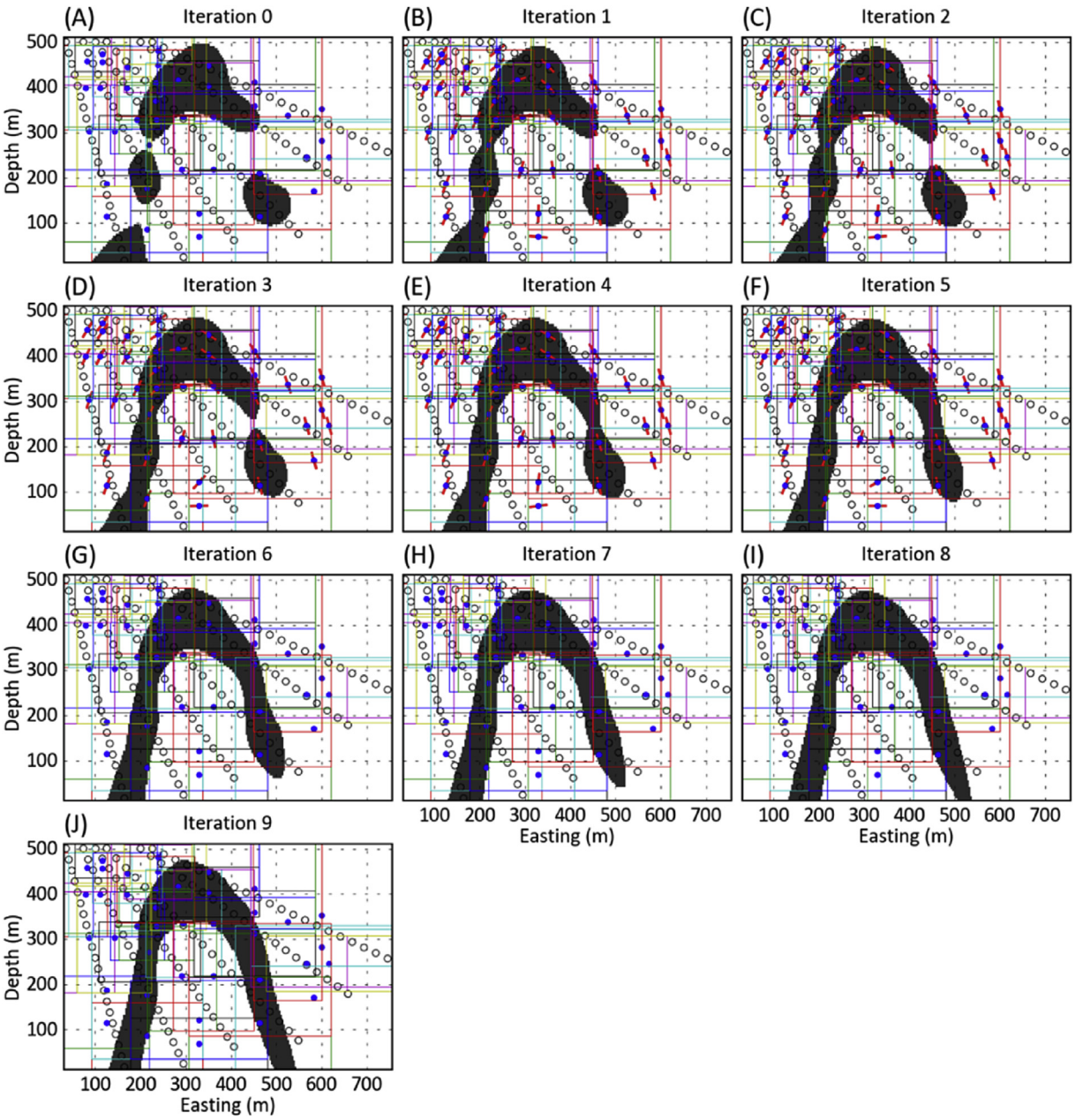

Fig. 6. Fully automatic PU RBF iterative refinements of the simplified boundary model from Fig. 3, starting with the isotropic model and ending with the locally anisotropic model. Iterative refinements are artificially limited to 11. Boxes indicate individual partition boundaries. Blue points represent the partition centers, and the associated red lines indicate the orientation of the local anisotropy inferred in each partition for each iteration. (For interpretation of the references to colour in this figure legend, the reader is referred to the web version of this article.)

weighted on overlapping sites:

$$s(\mathbf{x}) = \sum_{j=1}^{P} w_j(\boldsymbol{x}) s_j(\boldsymbol{x})$$

A key component of the PU is the weighting function that relates the local interpolants to the global. The weighting function is non-negative, zero at the boundaries and 1 at the center, and sums to 1 on overlapping sites (Pouderoux et al., 2004).

1.2. Modeling non-stationary geological features

Implicit modeling with realistic geological features is an important target for mineral resource estimation. Commercial implicit geological modeling software provides tools to manually incorporate more realistic local orientations of continuity (Cowan et al., 2003). Recently a framework to incorporate surface and off-surface orientations into RBF interpolation is developed to improve the implicit reconstruction of geological surfaces, mainly targeted for the sparse environment (Hillier et al., 2014). Tools such as locally varying anisotropy (LVA) kriging (Boisvert and Deutsch, 2011) or other second order non-stationarity interpolation methods (Fouedjio and Séguret, 2016; Machuca-Mory and Deutsch, 2013; Sullivan et al., 2007) can be applied to the SDF modeling workflow to account for curvilinear geological features.

A simplified example demonstrating the improvements possible by incorporating non-stationary interpolation (Boisvert and Deutsch, 2011) are shown in Fig. 2 and Fig. 3. The dipping drill holes sample two categories in the domain; samples of category 2 show the rough trace of an

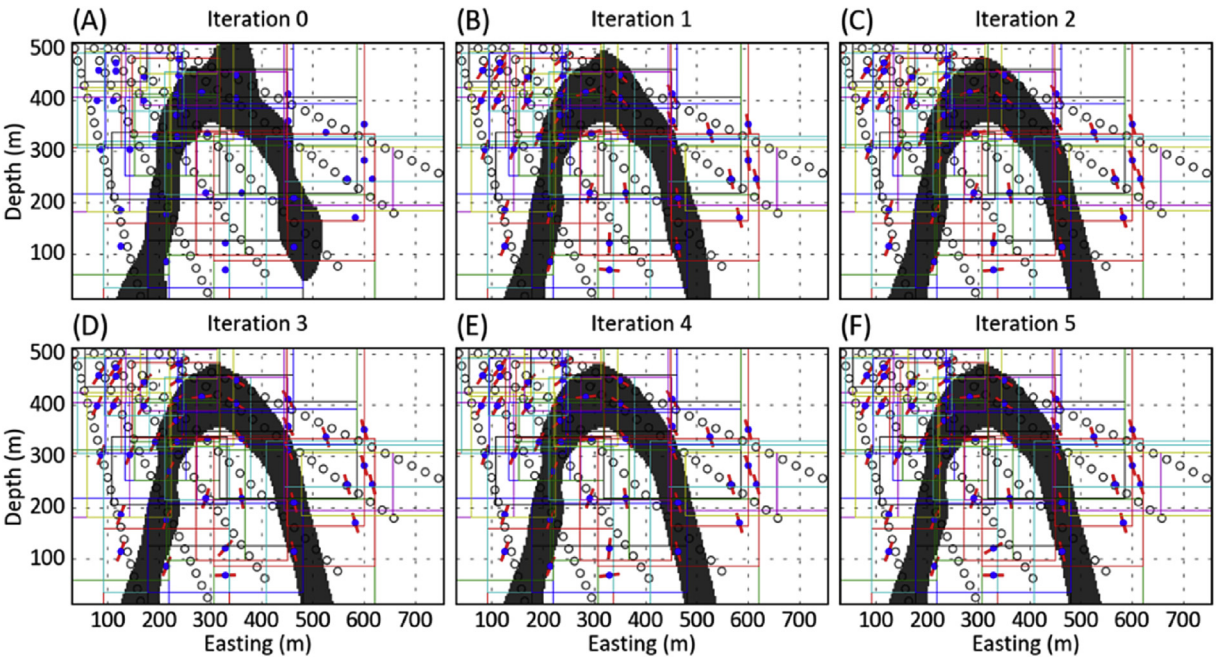

Fig. 7. Fully automatic PU RBF iterative refinements of the simplified boundary model starting with the anisotropic parameters modeled in Fig. 1. Boxes indicate individual partition boundaries. Blue points represent the partition centers, and the associated red lines indicate the orientation of the local anisotropy inferred in each partition for each iteration. (For interpretation of the references to colour in this figure legend, the reader is referred to the web version of this article.)

anticline feature, which is the main target of geological modeling (Fig. 3a). The SDF is calculated for category 2 at each location from the locations of each sample (Fig. 3b). The indicator variogram for category 2 is fitted with a spherical model, with a range of 173 m in the vertical direction and 124 m in the horizontal direction. The anisotropic ratios r_1 and r_2 are calculated from the relative lengths of the variogram model ranges: $r_1 = \frac{ahmin}{ahmax}$ and $r_2 = \frac{avert}{ahmax}$. The SDF is estimated with ordinary kriging to account for the locally varying mean. The target geological boundary is shown in white at the 0-level interface between the negative and positive areas in the exhaustive SDF model (Fig. 3c). This initial model is then used to infer a set of locally varying orientations required for LVA kriging (shown in Fig. 3d). Any method can be used to infer the locally varying orientations; in this work a multilevel gradient-PCA based method is used to extract the local features from the SDF model (Feng and Milanfar, 2002). A constant global anisotropic magnitude, $r_1 = 0.2$, is used to ensure the extracted structural orientations are enforced with LVA kriging. The final model generated with LVA kriging is shown in Fig. 3e. This 'refined' model has locally oriented boundaries that are more consistent with the interpreted shapes from the sampling of the domain. The inferred local orientations can be reviewed and modified by the expert to further iterate on the boundary model. However, LVA kriging becomes prohibitively computationally expensive for large datasets and large domains with complex structural features whereas the fast evaluation formulations for RBF interpolation can improve this process.

1.3. Proposed methodology

The proposed methodology is to improve boundary models with local anisotropy that is automatically extracted from the boundary models. The PU framework permits independent interpolation of each partition which is exploited by introducing locally anisotropic radial kernels. A gradient-PCA based method to extract orientations from the boundary models is used to define local orientations. There are 4 main steps:

1. Domain decomposition to define sets of data supported partitions for local interpolation.
2. Use the independent nature of the PU formulation to independently interpolate boundaries with the current anisotropy in each partition.
3. Use a method to extract the local orientations of continuity from the SDF or indicator models representing the target geological shapes.
4. Extract the most representative anisotropic orientation inside each partition, update partition parameters to include the new local anisotropy and repeat from step 2.

1.4. Domain decomposition

The ideal domain decomposition method simultaneously accounts for the data and the mesh the implicit function will be evaluated on. The goal of decomposition is to subdivide the domain based on the arrangement of the data into subdomains that have: similar quantities of data assigned to each; a reasonable collection of mesh (grid) locations to evaluate the local solution on; and valid weighting functions for the evaluation locations relative to the center of the partition (Fasshauer, 2007; Pouderoux et al., 2004). A number of domain partitioning algorithms can be used, including: a regular coarse grid; K-means; bisecting-K-means; binary tree; octree; and others (Klaas and Shephard, 2000; Pouderoux et al., 2004). The simplest partitioning is the regular coarse grid, which can work well for domains of roughly uniform sampling. However, a method that partitions based on the data arrangement is required in a mineral deposit setting where samples are irregularly distributed. The binary decomposition is used in this work since it can rapidly decompose a domain generating data supported partitions with the desired overlap and accounting for the axis-aligned set of grid locations with valid weighting functions (Pouderoux et al., 2004).

At each step in binary decomposition, a domain is split along the longest dimension into 2 overlapping sub-domains (Fig. 1a and b). In this work overlap is ensured in two ways: 1) during splitting a fraction of the data can be taken to be part of both child partitions so overlap is maintained along the boundary (Fig. 4b); and 2) after partitioning is finalized the partitions can be expanded beyond their original boundaries to

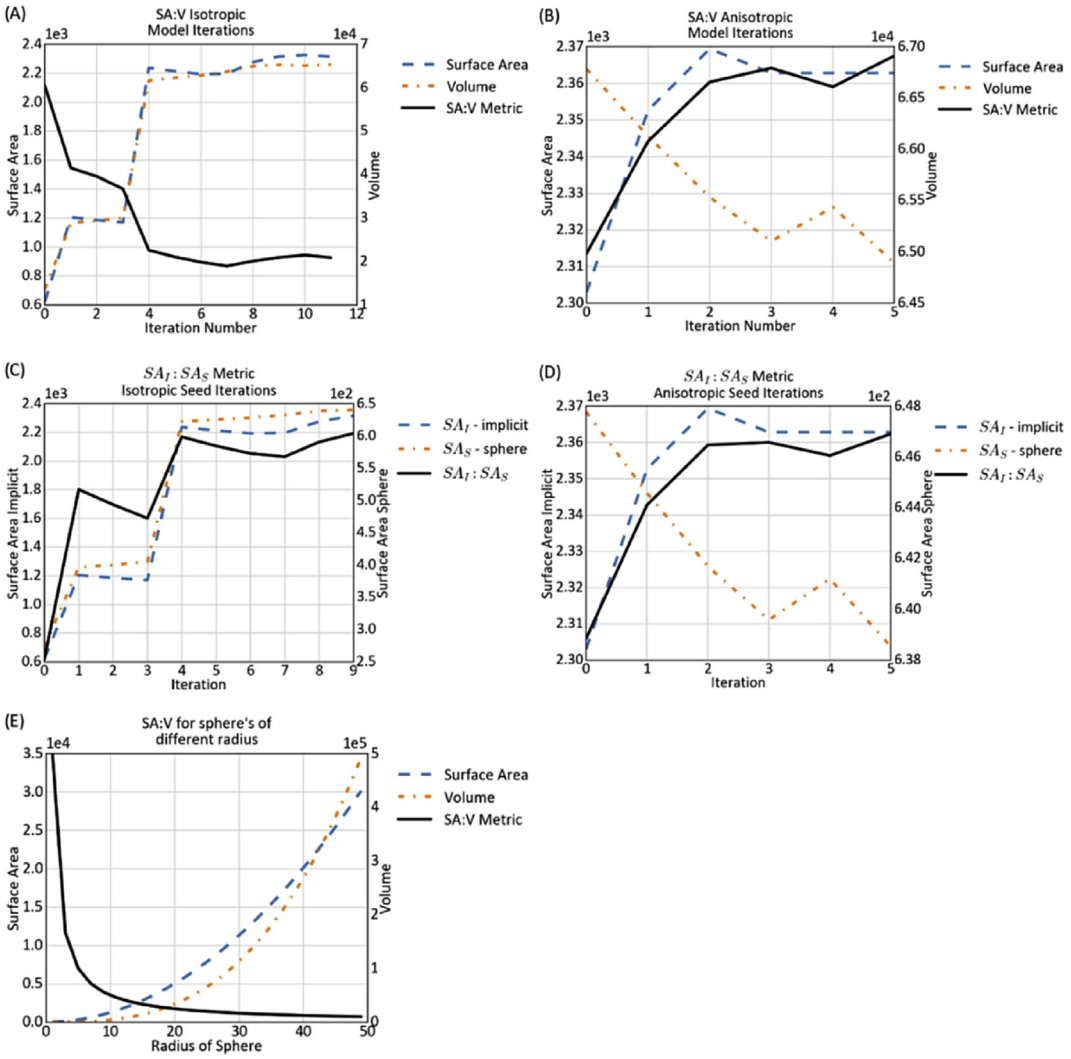

Fig. 8. The SA:V metric calculated on the A) isotropic and B) anisotropic seeded iterative refinements from Fig. 6 and 7, respectively. The SA:SA metric calculated on the C) isotropic and D) anisotropic seeded iterative refinements from Fig. 6 and 7, respectively. E) The SA:V metric calculated on a sphere of increasing radius – with increasing size of the object the SA:V of the object is minimized, motivating the use of the SA:SA metric in C) and D).

ensure suitable overlap when the data overlap is insufficient (Fig. 4d, e, f). In practice, both overlap methods are required since the data overlap alone can cause issues with recursion for some data configurations and the expansion overlap has potential to expand partitions to encompass too many data (e.g. cyan in Fig. 4c versus Fig. 4f). The binary decomposition is also relatively simple to implement and the resulting partitions have several valid weighting functions (Pouderoux et al., 2004):

$$C^0 : wf = 1 - d$$

$$C^1 : wf = 2d^3 - 3d^2 + 1$$

where d is the distance from the center of the partition to each cell in the partition, computed with (Pouderoux et al., 2004):

$$d = 1 - \prod_{p \in x,y,z} \frac{4*(\boldsymbol{x}_p - L_p)*(U_p - \boldsymbol{x}_p)}{(U_p - L_p)^2}$$

with $\boldsymbol{x}_p$ the coordinate of the current grid cell, L_p is the lower coordinate of the bounding box, and U_p is the upper coordinate of the bounding box, where the product is taken over each coordinate $p \in \{x, y, z\}$. Since the binary partitioning decomposition is only based on the number of data, there is no guarantee that the data allocated to each sub domain best reflects all grid cells allocated to that domain, for example, the data may exist only at 1 corner rather than being distributed uniformly throughout the partition.

1.5. Local support and local anisotropy

In the PU framework, subdomains are considered independent and the interpolation can be implemented in parallel (Cuomo et al., 2013). Moreover, a local support parameter for the kernel can be estimated from the data spacing in each sub-domain. The support parameter can be estimated from (Fasshauer, 2007):

$$\text{support} = \max_{\boldsymbol{x} \epsilon \Omega} \left[\min_{\boldsymbol{x}_j \epsilon X} \left\| \boldsymbol{x} - \boldsymbol{x}_j \right\|_2 \right]$$

where Ω represents the total set of grid locations, X represents the collection of data locations inside the domain and the resulting support distance can be interpreted as the radius of the largest empty circle or sphere that can be placed inside the bounds of each sub domain. The independent nature of partitions can be exploited to introduce local kernel properties to the implicit model (Casciola et al.,

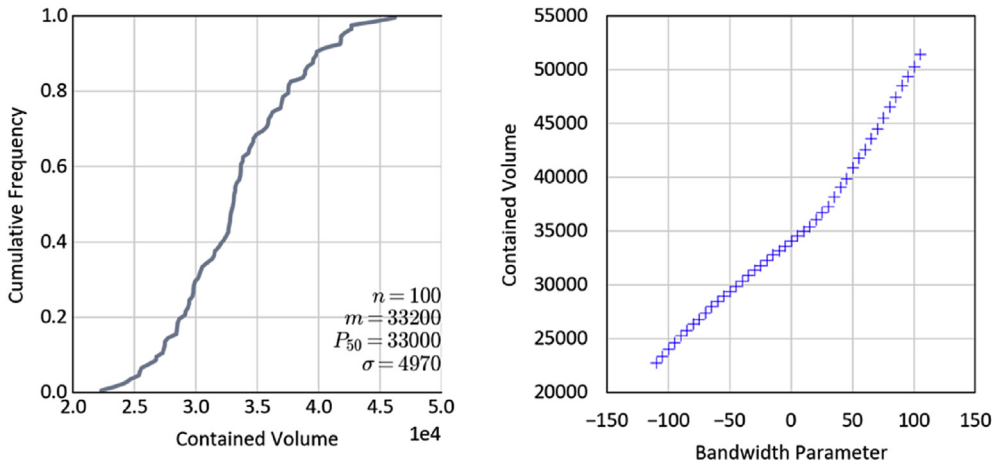

Fig. 9. Example distribution of uncertain volumes. Trained using the jackknife-based bandwidth-parameter, which can be mapped to the C-parameter to visualize contained volumes within the modeled geological solids.

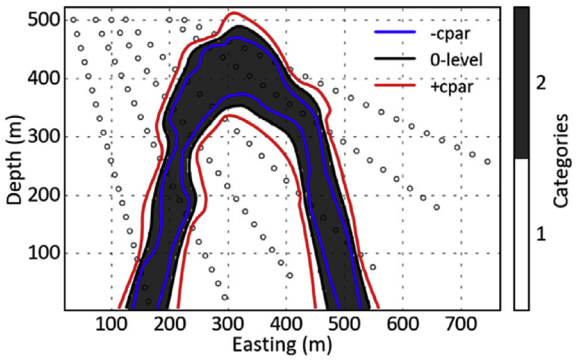

Fig. 10. Interpolated boundaries (black) showing the location of the lower and upper volume shells obtained with the bandwidth parameters calibrated in the jackknife-based framework of Wilde and Deutsch (2012).

2006). In this case, a set of anisotropic orientations and ranges derived from the local data can be used generate a locally anisotropic interpolation problem in each of the subdomains.

1.6. Modeling the local anisotropy

The gradient-PCA technique for local orientations from a gridded dataset developed by Feng and Milanfar (2002) is extended here to 3D to extract the dominant local orientations from boundary models. Readers interested in the 2D implementation of the gradient-PCA method are directed to Feng and Milanfar (2002). This technique generates a set of anisotropic orientations (strike and dip) from a gridded model that reflect the down-dip dominant orientation for a given window size at each location in the grid. The relative magnitudes of the singular values from singular value decomposition (SVD) can also be used as a preliminary estimate of the anisotropic magnitudes for each location in the domain, that is, the magnitudes reflect the dominance of an orientation in each decomposed gradient window. Since a partition is required to have a single set of anisotropic parameters, the estimated parameters for each location in the partition must be combined to a single representative set. In their implementation, Feng and Milanfar (2002) use the relative magnitudes of the singular values from SVD of the gradient matrix as a measure of the relative strengths of the orientations in each window, termed 'energy' and denoted by *ER*:

$$ER = \frac{sv_1 - sv_2}{sv_1 + sv_2}$$

where sv_1 and sv_2 are the singular values of the first and second principle axes, respectively. The energy calculated for each orientation estimate is then used to weight orientation estimates between layers in the multi-level algorithm, which is done specifically to deal with noisy input (Feng and Milanfar, 2002). For the current work, these energies are used to weight the orientation estimates in each partition to generate a single estimate such that dominant orientations contribute more than 'noisy' orientations to the averaged partition orientation.

For a given partition β, the vector representing the dominant orientation in the partition, $\vec{ori}_\beta$, has components $<\bar{x}, \bar{y}, \bar{z}>$ calculated by weighting the components of the orientation vectors estimated at each location within the partition:

$$\bar{x} = \sum_{i=1}^{ncell} ER_i x_i; \quad \bar{y} = \sum_{i=1}^{ncell} ER_i y_i; \quad \bar{z} = \sum_{i=1}^{ncell} ER_i z_i$$

$$\vec{ori}_\beta = \langle \bar{x}, \bar{y}, \bar{z} \rangle$$

$$\sum_{i=1}^{ncell} ER_i = 1$$

where *ncell* is the total number of estimation locations within the current partition, and ER_i is the energy calculated from the singular values from SVD at each estimation location. In 3D, the orientation extraction algorithm is limited to extracting the dip-direction and dip components of the local orientations (plunge = 0). Taking the weighted average of the vector components while ensuring the axial nature of the orientations are accounted for is a suitable method to compute an average orientation in each partition for gentle to moderately dipping terrains (Lillah and Boisvert, 2015; Machuca-Mory et al., 2015). However, for 90° plunging structures, vector averaging of these vectors cannot compute an average partition anisotropy. The extrapolated partition orientation represents the most dominant orientation according to the estimation energies from the local gradient windows. For cases where partitions encompass many structurally predominant orientations, this weighting scheme may generate a nonsensical partition orientation, since no single orientation may adequately describe the dominant orientations in the partition. In this case splitting the offending partition, or considering fewer data-per-partition initially may help to alleviate these problems. Alternatively, a reasonable orientation could be assigned by considering the surrounding

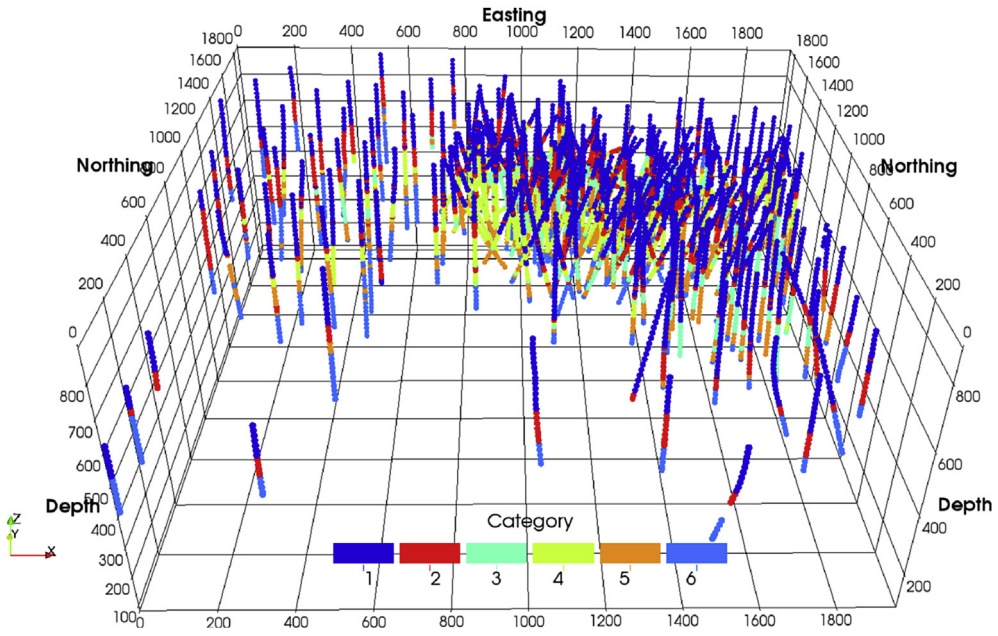

Fig. 11. Rock types and drill hole locations, oblique view looking north.

partitions.

The proposed weighting method uses the magnitude of the singular values to estimate the dominant orientations. Since the anisotropic magnitudes are also estimated from the relative lengths of the singular values (i.e. r1 $= \frac{sv_2}{sv_1}$ and r2 $= \frac{sv_3}{sv_1}$) this weighting scheme cannot be used to obtain the dominant anisotropic magnitude. Instead, the arithmetic average of the magnitudes is taken for the partition. A more representative estimate of the local magnitudes of anisotropy could be obtained by fitting locally weighted variograms and extracting the model ranges as in Machuca-Mory and Deutsch (2013).

The anisotropic angles and ranges are introduced to the local interpolation problem by computing anisotropic distances using rotation matrices. First, the angles required for the rotation matrix are calculated from the components of the partition anisotropy vector computed above:

$$\begin{bmatrix} \alpha \\ \beta \\ \phi \end{bmatrix} = \begin{bmatrix} \arctan 2(\bar{x},\ \bar{y}) \\ \arcsin(\bar{z}) \\ 0 \end{bmatrix}$$

And the rotation matrix is calculated, as in Rossi and Deutsch (2014, pp 42):

$$R = \begin{bmatrix} \cos\alpha\cos\phi - \sin\alpha\sin\beta\sin\phi & -\sin\alpha\cos\phi - \cos\alpha\sin\beta\sin\phi & \cos\beta\sin\phi \\ r_1{*}\sin\alpha\cos\beta & r_1{*}\cos\alpha\cos\beta & r_1{*}\sin\beta \\ r_2{*}(-\cos\alpha\sin\phi - \sin\alpha\sin\beta\cos\phi) & r_2{*}(\sin\alpha\sin\phi - \cos\alpha\sin\beta\cos\phi) & r_2{*}\cos\beta\cos\phi \end{bmatrix} \quad (2)$$

Using the rotation matrix the points in the domain are rotated to have the correct anisotropic relationships with:

$$\begin{bmatrix} x_r \\ y_r \\ z_r \end{bmatrix} = R\cdot \begin{bmatrix} x_o \\ y_o \\ z_o \end{bmatrix} \quad (3)$$

where $\boldsymbol{x}_o$ are the original locations, and $\boldsymbol{x}_r$ are the rotated locations that have the desired anisotropic relationships. Finally, the Euclidean distance computed in the rotated space (e.g. $||\boldsymbol{x}_{ri} - \boldsymbol{x}_{rj}||_2$) is used in equation (1) to train and evaluate the locally anisotropic interpolants.

1.7. Iterative refinements and speeding up iterative implicit modeling

The final component of the proposed iterative refinements is to choose a criterion indicating the refinements are complete. Here, the number of blocks changed between iterations is taken as a measure of 'refinement' between iterations. If a block is estimated as 'inside' in one iteration, and 'outside' in another iteration, it is considered to be changed. Initially many blocks will change designation, but this is expected to decrease with continued iteration. A tolerance can be set to stop refinements of the partitions if there is insufficient change between iterations. Since the partitions are independent, if refinement of a partition results in no beneficial changes, then further refinement of that partition is unnecessary, and the partition can be omitted from the global solution step in the boundary interpolation, which can drastically speed up the boundary refinement algorithm.

1.8. Multiple category implicit modeling

Silva (2015) introduced a methodology to simultaneously model N-categories using the SDF implicit modeling workflow presented above.

By obtaining an interpolated SDF value for each category, as described above, the N-category implicit model is constructed by choosing the category with the most negative interpolated SDF at each location. A simple test domain with 3 categories, shown in Fig. 5a, is used to demonstrate the extraction of the categorical model from the individual interpolated SDF models. The interpolated SDF for each category 1, 2 and 3 are shown in Fig. 5b, c, and d, respectively; each SDF is interpolated independently with an isotropic Gaussian kernel. The final merged categorical model is shown in Fig. 5e. The category prevailing at each location is chosen by taking the category corresponding to the minimum

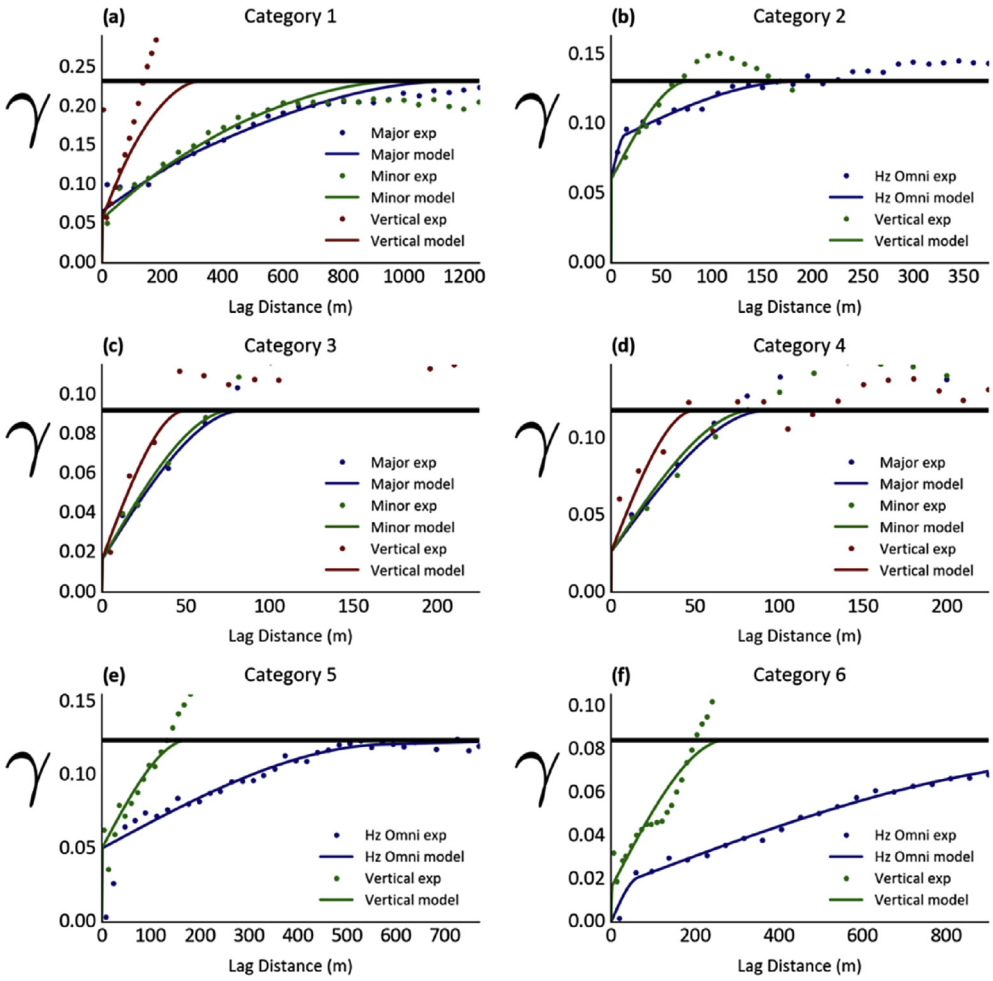

Fig. 12. Experimental and model variograms for each category.

Table 1
Modeled global anisotropic parameters for each category from variograms in Fig. 10.

Category	Anisotropic Angles			r_1	r_2
	strike	dip	plunge		
1	90	15	0	0.89	0.27
2	125	15	0	1.0	0.39
3	270	70	0	0.91	0.18
4	270	75	0	0.87	0.51
5	55	5	0	1.00	0.33
6	45	5	0	1.00	0.28

2. Synthetic example

The locally anisotropic synthetic dataset presented in Fig. 3 is used to demonstrate the proposed iterative refinement framework. Two seed models are considered; 1) an isotropic SDF model; and 2) a globally anisotropic model. In the first example, the starting model contains several disconnected 'blobs' (Fig. 6a). The first few sets of orientation refinements generate anisotropic properties that poorly reflect the expected orientation of the two limbs (Fig. 6b and c). The tolerance for stopping in this example is set extremely low to ensure that refinements are made for each partition in each iteration regardless of the amount of change. By iteration 4 (Fig. 6e) the local boundaries better reflect the expected configuration and by iteration 8 (Fig. 6i) the true down-dip continuity and thickness on each limb is reproduced. In this case the main structure of the domain is mostly achieved by iteration 4 and perhaps at this stage the iterative refinements could be stopped manually.

Iterative refinements from a globally anisotropic seed model are shown in Fig. 7. By constraining the starting model to better represent the locally anisotropic properties, the iterative refinements more quickly arrive at a realistic boundary model with the desired down-dip continuity and thickness. Seeding the iterative refinement with the best set of global anisotropic parameters can speed up interpolation and helps ensure the correct locally anisotropic properties are extracted from the model.

2.1. On the 'goodness' of an implicit model

The evaluation of the locally anisotropic model is largely qualitative; the boundary model is subjectively improved through increased geological reproduction given the interpretation of the domain. Incorporating LVA to the interpolation step of boundary modeling will improve the cross-validation results since LVA increases the relatedness of nearby samples (Boisvert and Deutsch, 2011). However, for the present applications improved cross validation does not translate to a better implicit geological model.

A very simple but quantifiable metric of 'goodness' for the implicit shape is proposed. The metric is derived from subjective qualities of an implicit model that are targets of the geomodeler during model construction. The metric can be calculated for any boundary model, and can be used to compare different models objectively, either between modelers or between iterations of the same model.

There are two forms of the proposed metric which are both derived from the ratio of the surface area to the volume of the implicit model. This metric can be justified as an indicator of 'goodness' since poorly parameterized implicit models tend to exhibit bubble, balloon or sphere-

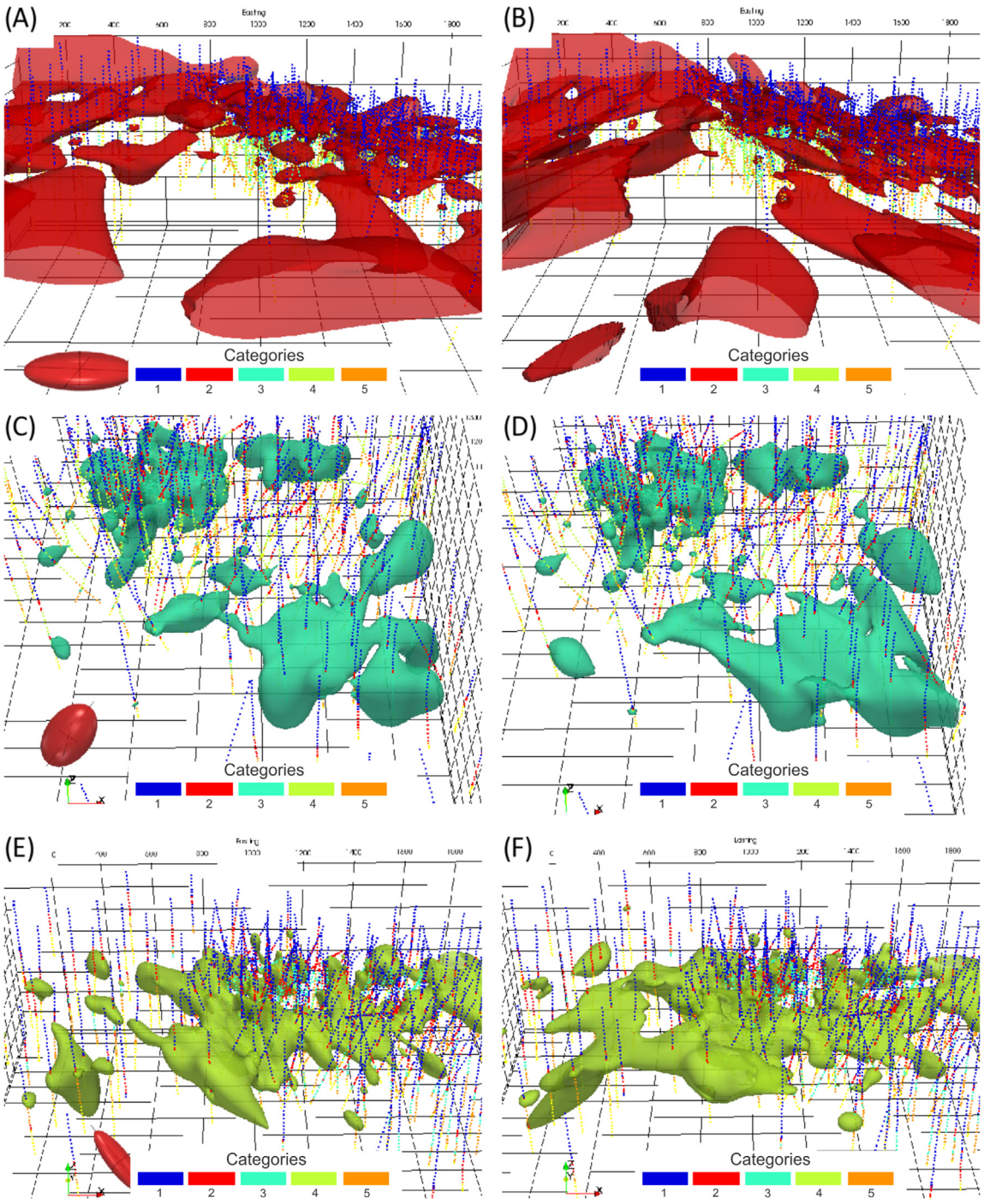

Fig. 13. Comparison of the boundaries for category 2, 3 and 4 modeled with A), C), and E) global anisotropy. Red ellipsoid shows the global anisotropy used in each interpolation in A), C) and E). Automatic local anisotropy refinements shown in B), D) and F). (For interpretation of the references to colour in this figure legend, the reader is referred to the web version of this article.)

like shapes that do not represent realistic geological features (e.g. Fig. 6a). Such models are typically modified by considering anisotropy to improve the continuity of the model in different directions to more accurately represent the underlying geological features (e.g. Fig. 7a). However, even in the case of Fig. 7a improvements to the implicit model in the form of fewer bubble-like shapes could be made. To compute the metric, the surface area and volume of each disconnected region in the model are calculated. For example, in Fig. 6a there are 3 disconnected regions and in Fig. 6b there are 2 disconnected regions. For each disconnected region in the implicit model, the SA:V of the region is computed (Fig. 8a and b). For a constant number of connected regions, the SA:V of the implicit shape tends to increase as the boundary becomes more locally representative (Fig. 8b). Notably, when the implicit model starts with disconnected regions that become connected, the volume is increasing which tends to minimize the SA:V (Fig. 8a), which is true even for a sphere (Fig. 8e). In this case it is more useful to compute the ratio of SA:V implicit model to the SA:V of the sphere with equivalent volume. The metric is then defined by:

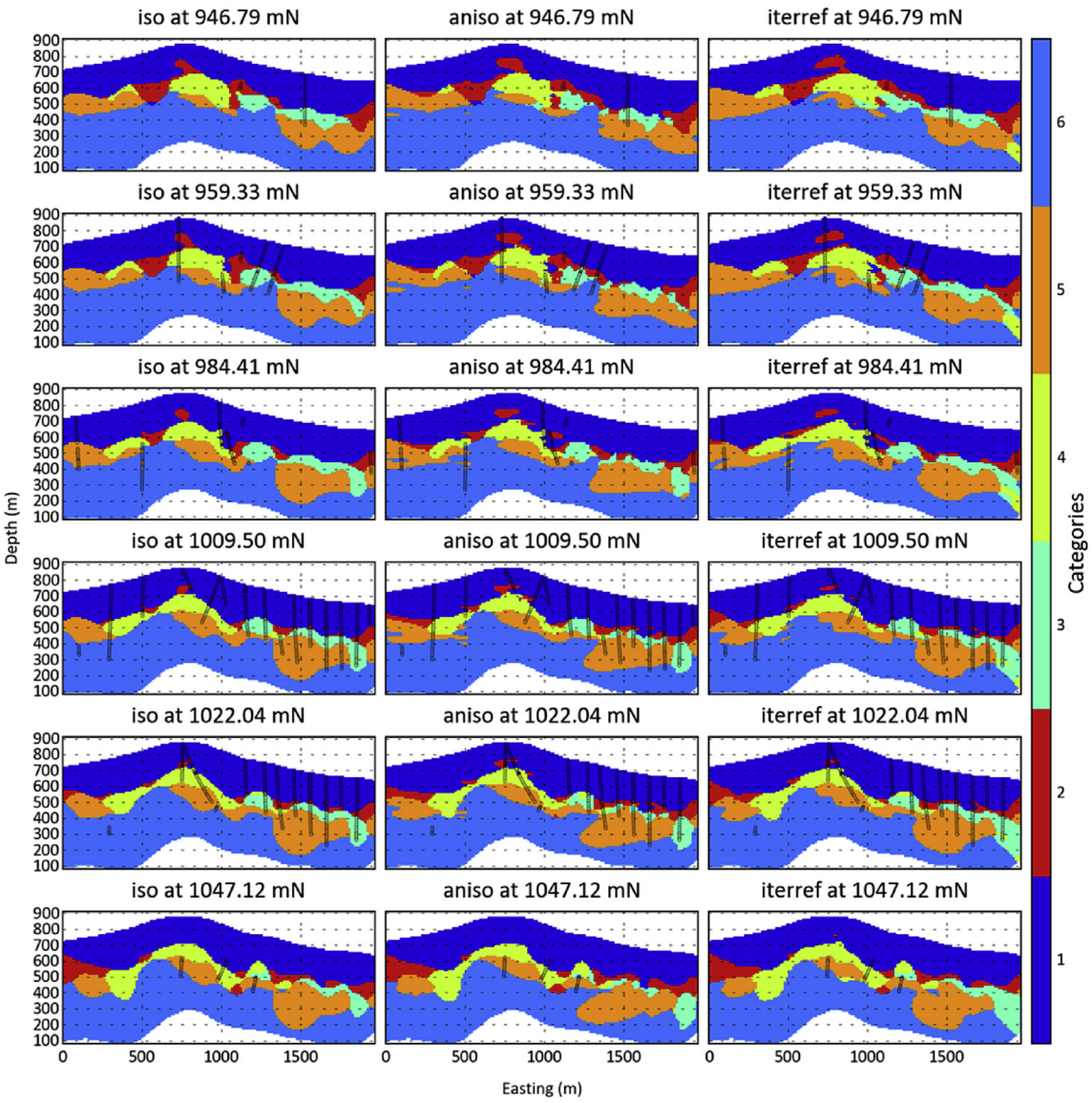

Fig. 14. X-Z slices through sparsely sampled southern portions of the domain. ('iso'), globally anisotropic ('aniso') and locally anisotropic ('iterref') parameters. Data locations are shown.

$$M = \frac{\frac{SA_{implicit}}{V_{implicit}}}{\frac{SA_{sphere}}{V_{sphere}}}$$

And when $V_{implicit} = V_{sphere}$:

$$M = \frac{SA_{implicit}}{SA_{sphere}}$$

These two metrics are shown in Fig. 8c and d. The tendency of an implicit modeling project, then, is to have models that start out with balloon-like spherical shapes where the boundaries may be disconnected and $SA_{implicit}$ locally approximates SA_{sphere}. Then, with further refinements and modeling iterations, the models progress to have fewer disconnected regions with less rounded balloon like shapes. The above metrics are computed on the iterations in Fig. 6 and shown in Fig. 8.

3. Volumetric uncertainty

There may be significant volumetric uncertainty present in implicit models owing to uncertainty in the location of the boundaries, and capturing this uncertainty is an important component of the geostatistical workflow. Volumetric uncertainty describes the variability in the volume of material encompassed by a modeled geo-solid. Since the SDF interpolated to the unsampled locations controls the location of the boundary, the volumetric uncertainty is quantified by changing, in some way, the underlying volumetric function or modifying the modeling parameters that interpolate the SDF to the unsampled locations. Various methods are proposed to quantify this uncertainty, including: calibrating bandwidth parameters and simulating unconditional realizations to truncate the uncertain zone to generate boundary realizations (Wilde and Deutsch, 2012); considering uncertain structural orientation inputs to the model construction and assessing the probability to be inside or outside over a number of realizations (Lindsay et al., 2012); considering uncertain proportions in the form trend models (Hadavand and Deutsch, 2017); resampling tops and bottoms within uncertain zones of a modeled ore solid to generate realizations of thickness (Yamamoto et al., 2015); or directly simulating the volumetric function within the constraints of a non-stationary and geologically realistic LVA framework (Lillah and Boisvert, 2013). There are many methods that can be used to obtain the distribution of uncertain volumes for a given geological model. In this work the bandwidth parameter from Wilde and Deutsch (2012) is trained with local anisotropy by applying the jackknife-based workflow to assess misclassification with increasing bandwidth parameter. The final step

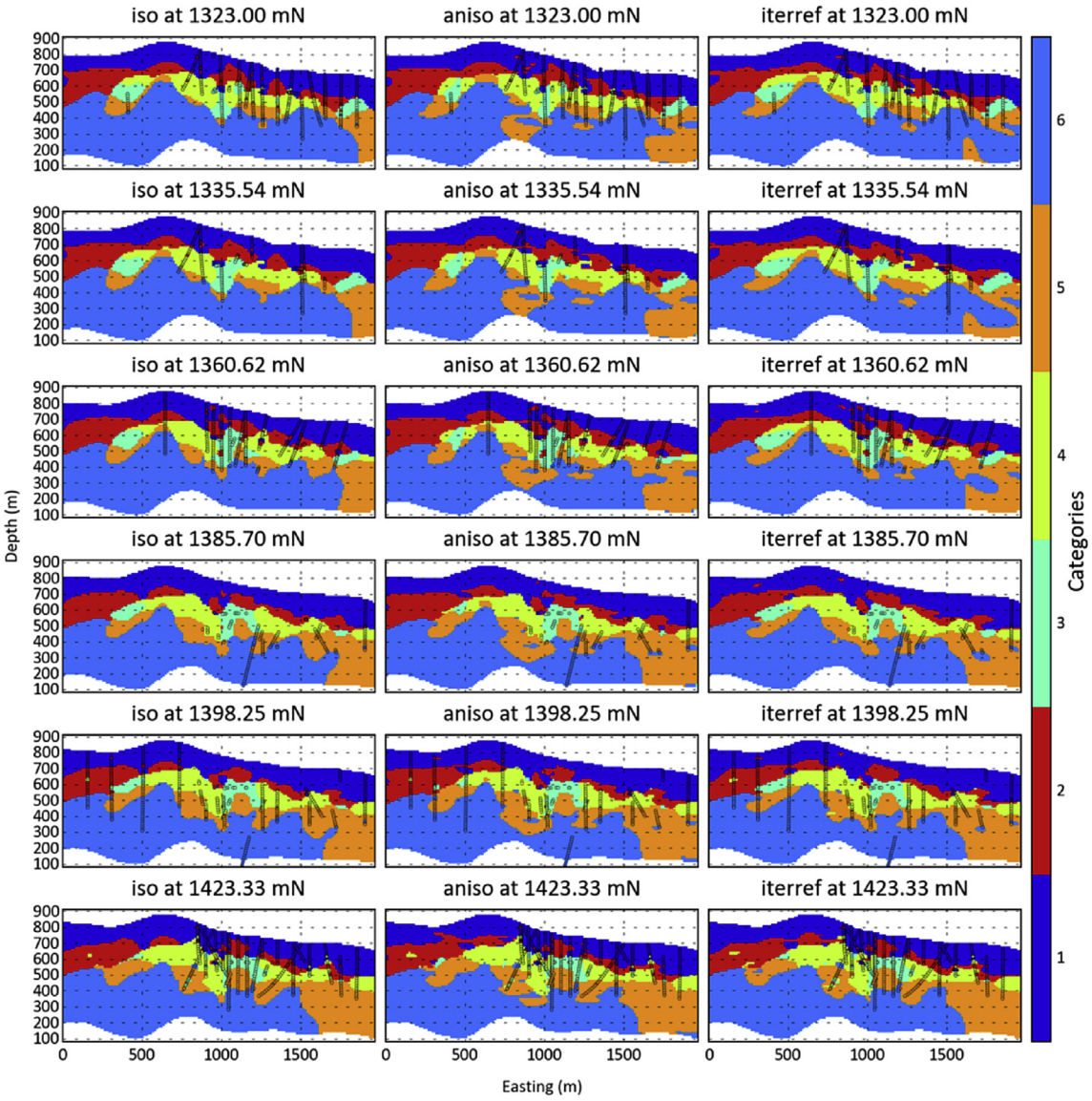

Fig. 15. X-Z slices through models constructed with globally isotropic ('iso'), globally anisotropic ('aniso') and locally anisotropic ('iterref') parameters. Data locations are shown.

after quantifying the volumetric uncertainty is to generate realizations of the boundary models and extract iso-probability contours for the domain for different uncertain volume distributions (Fig. 9 and Fig. 10).

The process is illustrated in Figs. 9 and 10. The volumetric uncertainty is acquired by one of the methods above, for example, that from Wilde and Deutsch (2012). The volumetric uncertainty can be mapped to sets of bandwidth parameters that constrain the different volumes, and the different volumetric shells can be viewed (as in Fig. 10).

4. Case study

A dataset of 8527 samples from 316 drill holes that sample a large Cu-porphyry deposit are used to illustrate the proposed methodology. Six rock types are the target of geological modeling; categories 3 and 4 are the main modeling targets considering the areas of dense drilling and the contained grades (Fig. 11). Category 3 has the highest average grades and is mainly localized to the northeast portion of the domain. Category 4 occurs at the periphery of category 3 and has similar grade distributions. The dense drilling in the domain to the northeast mainly targets category 3 whereas category 4 has a more consistent distal extent to this densely-drilled area. Together with category 2, which also has elevated grade values, these lithologies comprise a significant proportion of the samples ($p_2 + p_3 + p_4 = 0.411$). Category 1 and 6 form the unmineralized top and bottom of the modeling domain respectively. Category 2 and 5 are related to the main mineralized lithologies; category 2 tends to be located above the main mineralized categories, whereas category 5 is mostly found below 3 and 4.

An isotropic model is generated for inspection to interpret any predominant continuities in the domain prior to modeling anisotropy with experimental variograms. An isotropic Gaussian kernel is used with the local support estimated from the data spacing in each partition. The partitioning algorithm was specified to have 100 data-per-partition, with a final overlap of 50% in each of the x, y and z directions.

Global anisotropic parameters (strike, dip, plunge, r_1 and r_2) for each category are determined from the model variograms fitted to the experimental indicator variograms calculated along the directions of maximum continuity inferred from the isotropic model (Fig. 12). The extracted anisotropic parameters for RBF interpolation are shown in Table 1. As described above, the anisotropic parameters strike, dip, plunge, r_1 and r_2 are utilized in the SDF interpolation for each category by computing the corresponding rotation matrix using equation (2), and scaling the data and mesh locations independently for each SDF interpolation (for each category) to have the correct anisotropic properties using equation (3). For example for 6 categories, 6 rotation matrices and

location scaling are required to represent to interpolate the globally anisotropic SDF for each category.

The final set of boundaries are generated by considering the fully automatic refinement algorithm proposed in this work. The iterative refinements are performed on each lithology by seeding the algorithm with the globally anisotropic model with the same partitioning parameters used in all runs. The final N-category implicit model is generated in the post processing workflow described above (Fig. 5; Silva, 2015). At this stage, the geological crosscutting relationships could be incorporated to ensure that the domain honors known relationships indicated by superposition.

Three-dimensional boundary shells considering global anisotropy extracted from the gridded SDF are shown in Fig. 13a, c and e. The boundaries smoothly honor the data locations within the partitioning framework considering the global anisotropy. After inspecting this model, it is likely that refinement of the variogram model would be performed or sub domaining applied to separate zones with distinct local anisotropic properties. Specifically for category 3 and 4, the highest continuity modeled from the variograms is steeply dipping and variably oriented (Fig. 13c and e). This anisotropy is over exaggerated in places and most likely the parameters for these categories should be revisited to ensure they correctly account for the geological interpretation of the domains. For category 2, the contrasting anisotropic properties at the west and east end of the modeling domain are not adequately captured with the global anisotropic model (Fig. 13a).

Boundary shells considering the local partition anisotropy are shown in Fig. 13b, d and f. These locally anisotropic models are notably different than the globally anisotropic model. For example, consider the geometry of category 2 in Fig. 13b. The basement rocks (category 6) form an upwelling-intrusive like feature just to the west of the dense drilling, which corresponds to the topographic high; the result is that units above are dipping locally in opposite directions, as shown in Fig. 13b. The freedom of the local anisotropic properties allows the boundaries to honor the local dips which are inferred from the data. For regions with limited data, the framework also appears to extrapolate adequately according to the automatically inferred orientations (Fig. 13f). Similar conclusions can be drawn for category 3 (Fig. 13d); the main section with dense drilling the northwest portion of the figure remains relatively isotropic, whereas there is anisotropy inferred in southeast, according to the local geometry implied by the data. Similarly the anisotropy inferred from the global variogram model for category 4 provides a limited interpretation (Fig. 13e). In the locally anisotropic model the main continuity is dipping west on the west side of the up-welling feature, whereas to the east the continuity is dipping to the east (Fig. 13f). This provides a more reasonable model based on the geological interpretation.

A set of E-W oriented slices generated with globally isotropic, globally anisotropic and locally anisotropic methods are shown in Fig. 14 and Fig. 15. The set of slices in Fig. 14 generally correspond to the more southern portions of the domain where sparse information is present, whereas Fig. 15 shows slices through the densely-sampled regions. The set of slices show that using the isotropic model in the presence of dense drill information adequately reproduces the geometric relationships (left column, Fig. 15). However, for sparser regions, the continuity of the main zones is enhanced in the locally anisotropic case when compared with the isotropic and globally anisotropic cases (Fig. 14). For the densely-sampled regions, local improvements are made in the locally anisotropic case but they are subdued from the additional constraints from surrounding data (Fig. 15).

The iteratively refined local anisotropic boundaries better reflect the geological interpretation of the domain as the units have locally varying orientations that reflect the interpreted draping on either side of the central upwelling feature. Out of the three methods, the locally anisotropic boundaries provide the expert with the best starting point for interpretation. In general, considering the 'geological reasonability' of the resulting shapes on a set of 2D sections is limited and should be used with caution. All interpretations should be made in 3D, or in 2D considering the between-section relationships. It should also be noted that the effects of automatically inferred local anisotropy may be more restricted where there is significant data density to control the boundary geometry. This can be seen in Figs. 13c and 11d where in the presence of dense drilling in the northeast portion of the property, the resulting boundary models are similar between the two different methods. However, in the south and west portions of the domain where data density is sparser, the interpretation is more varied according to the local data and the changing anisotropic properties.

5. Conclusions

The proposed methodology provides the expert a better starting point for modeling geology with locally varying features for complex geological datasets in the presence of sufficient sample density. The proposed methodology to automatically infer local anisotropy from the data is similar to a 'bootstrap' workflow since a better model is constructed by considering features extracted from previous models. The methodology is simple and flexible, providing the expert a straight forward method to manually infer and incorporate local anisotropy. Indeed, the local orientation extraction algorithm could be paired with the orientation constraints of Hillier et al. (2014) with a greedy algorithm to generate locally anisotropic boundary models with iteratively introduced anisotropic properties.

Often implicit modeling is used to infer a single geological model, but if a global distribution of uncertainty is known, the proposed automatic modeling technique can be used to generate N-realizations of geology calibrated to the global uncertainty. This is important for deposits with large geological uncertainties.

Acknowledgements

The authors would like to thank the member companies of the Center for Computational Geostatistics (CCG) for their support of this research.

References

Beatson, R.K., Cherrie, J.B., Mouat, C.T., 1999. Fast Fitting of radial basis functions: methods based on preconditioned GMRES iteration. Adv. Comput. Math. 11, 253–270. http://dx.doi.org/10.1023/A:1018932227617.

Beatson, R.K., Light, W.A., Billings, S., 2001. Fast solution of the radial basis function interpolation equations: domain decomposition methods. SIAM J. Sci. Comput. 22 (5), 1717–1740.

Boisvert, J.B., Deutsch, C.V., 2011. Programs for kriging and sequential Gaussian simulation with locally varying anisotropy using non-Euclidean distances. Comput. Geosci. 37 (4), 495–510. http://dx.doi.org/10.1016/j.cageo.2010.03.021.

Carr, J.C., Beatson, R.K., Cherrie, J.B., Mitchell, T.J., Fright, W.R., McCallum, B.C., Evans, T.R., 2001. Reconstruction and representation of 3D objects with radial basis functions. In: Proceedings of the 28th Annual Conference on Computer Graphics and Interactive Techniques, pp. 67–76. http://dx.doi.org/10.1145/383259.383266.

Casciola, G., Lazzaro, D., Montefusco, L.B., Morigi, S., 2006. Shape preserving surface reconstruction using locally anisotropic radial basis function interpolants. Comput. Math. Appl. 51, 1185–1198. http://dx.doi.org/10.1016/j.camwa.2006.04.002, 8 SPEC. ISS.

Cowan, J., 2014. "X-ray Plunge Projection"— Understanding Structural Geology from Grade Data "X-ray Plunge Projection"— Understanding Structural Geology from Grade Data. In: AusIMM Monograph 30 Mineral Resource and Ore Reserve Estimation — The AusIMM Guide to Good Practice, vol. 2, pp. 207–220.

Cowan, E.J., Beatson, R.K., Ross, H.J., Fright, W.R., McLennan, T.J., Evans, T.R., Carr, J.C., Lane, R.G., Bright, D.V., Gillman, A.J., Oshust, P.A., 2003. Practical implicit geological modelling. In: Fifth International Mining Geology Conference, pp. 17–19.

Cuomo, S., Galletti, A., Giunta, G., Starace, A., 2013. Surface reconstruction from scattered point via RBF interpolation on GPU. In: Computer Science and Information Systems (FedCSIS), 2013 Federated Conference on, pp. 433–440.

Fasshauer, G.E., 2007. Meshfree Approximation Methods with MATLAB, vol. 6. World Scientific.

Fazio, V.S., Roisenberg, M., 2013. Spatial interpolation: an analytical Comparison between kriging and RBF networks. In: Proceedings of the 28th Annual ACM Symposium on Applied Computing. ACM Press, Coimbra, Portugal, pp. 2–7. http://dx.doi.org/10.1145/2480362.2480364.

Feng, X., Milanfar, P., 2002. Multiscale Principal Components Analysis for Image Local Orientation Estimation. In: Proceedings of the Thirty-sixth Asilomar Conference on Signals, Systems and Computers, vol. 1, pp. 478–482. http://dx.doi.org/10.1109/ACSSC.2002.1197228. JOUR.

Fouedjio, F., Séguret, S., 2016. Predictive geological mapping using closed-form non-stationary covariance functions with locally varying anisotropy: case study at El Teniente Mine (Chile). Nat. Resour. Res. 1–13. http://dx.doi.org/10.1007/s11053-016-9293-4.

Hadavand, M., Deutsch, C.V., 2017. Facies proportion uncertainty in presence of a trend. J. Petroleum Sci. Eng. 153, 59–69.

Hillier, M.J., Schetselaar, E.M., de Kemp, E.A., Perron, G., 2014. Three-dimensional modelling of geological surfaces using generalized interpolation with radial basis functions. Math. Geosci. 931–953. http://dx.doi.org/10.1007/s11004-014-9540-3.

Journel, A.G., 1989. Fundamentals of Geostatistics in Five Lessons, vol. 8. American Geophysical Union, Washington, DC, p. 40.

Klaas, O., Shephard, M.S., 2000. Automatic generation of octree-based three-dimensional discretizations for Partition of Unity methods. Comput. Mech. 25 (2–3), 296–304. http://dx.doi.org/10.1007/s004660050478.

Knight, R.H., Lane, R.G., Ross, H.J., Abraham, A.P.G., Cowan, J., 2007. Implicit ore delineartion. In: Proceedings of Exploration 07: Fifth Decennial International Conference on Mineral Exploration, pp. 1165–1169.

Lajaunie, C., Courrioux, G., Manuel, L., 1997. Foliation fields and 3D cartography in geology: principles of a method based on potential interpolation. Math. Geol. 29 (4), 571–584. http://dx.doi.org/10.1007/BF02775087.

Lillah, M., Boisvert, J.B., 2013. Stochastic distance based geological boundary modeling with curvilinear features. Math. Geosci. 45, 651–665.

Lillah, M., Boisvert, J.B., 2015. Inference of locally varying anisotropy fields from diverse data sources. Comput. Geosci. 82, 170–182. http://dx.doi.org/10.1016/j.cageo.2015.05.015.

Lindsay, M.D., Aillères, L., Jessell, M.W., de Kemp, E.A., Betts, P.G., 2012. Locating and quantifying geological uncertainty in three-dimensional models: analysis of the Gippsland Basin, southeastern Australia. Tectonophysics 546–547, 10–27. http://dx.doi.org/10.1016/j.tecto.2012.04.007.

Lorensen, W.E., Cline, H.E., 1987. Marching cubes: a high resolution 3D surface construction algorithm. ACM SIGGRAPH Comput. Graph. 21 (4), 163–169.

Machuca-Mory, D.F., Deutsch, C.V., 2013. Non-stationary geostatistical modeling based on distance weighted statistics and distributions. Math. Geosci. 45 (1), 31–48. http://dx.doi.org/10.1007/s11004-012-9428-z.

Machuca-Mory, D.F., Rees, H., Leuangthong, O., 2015. Grade modelling with local anisotropy angles: a practical point of view. In: 37th Application of Computers and Operations Research in the Mineral Industry (APCOM 2015).

Ohtake, Y., Belyaev, A., Seidel, H.P., 2003. A multi-scale approach to 3D scattered data interpolation with compactly supported basis functions. In: Shape Modeling International, 2003, pp. 153–161. http://dx.doi.org/10.1109/SMI.2003.1199611.

Ohtake, Y., Belyaev, A., Seidel, H.P., 2006. Sparse surface reconstruction with adaptive Partition of Unity and radial basis functions. Graph. Models 68 (1), 15–24. http://dx.doi.org/10.1016/j.gmod.2005.08.001.

Pouderoux, J., Gonzato, J.C., Tobor, I., Guitton, P., 2004. Adaptive hierarchical RBF interpolation for creating smooth digital elevation models. In: Proceedings of the 12th Annual ACM International Workshop on Geographic Information Systems - GIS 04, p. 232. http://dx.doi.org/10.1145/1032222.1032256.

Rossi, M.E., Deutsch, C.V., 2014. Mineral Resource Estimation, , first ed.vol. 1). Springer Science. http://dx.doi.org/10.1007/978-1-4020-5717-5.

Silva, D.A., 2015. Enhanced Geologic Modeling with Data-driven Training Images for Improved Resources and Recoverable Reserves. Unpublished PhD Thesis. University of Alberta, Edmonton, p. 246.

Sullivan, J., Satchwell, S., Ferrax, G., 2007. Grade estimation in the presence of trends—the adaptive search approach applied to the Andina Copper Deposit, Chile. In: Proceedings of the 33rd International Symposium on the Application of Computers and Operations Research in the Mineral Industry. GECAMIN Ltd, pp. 135–143, 2007.

Vollgger, S.A., Cruden, A.R., Aillères, L., Cowan, J., 2015. Regional dome evolution and its control on ore-grade distribution: insights from 3D implicit modelling of the Navachab gold deposit, Namibia. Ore Geol. Rev. 69, 268–284. http://dx.doi.org/10.1016/j.oregeorev.2015.02.020.

Wilde, B.J., Deutsch, C.V., 2012. Kriging and simulation in presence of stationary domains: developments in B. In: Quantitative geology and Geostatistics, vol. 17, p. 12. Oslo.

Xiaojun, W., Michael, Y., Wang, Q.X., 2005. Implicit fitting and smoothing using radial basis functions with partition of unity. In: Proceedings - Ninth International Conference on Computer Aided Design and Computer Graphics, CAD/CG 2005, pp. 139–148. http://dx.doi.org/10.1109/CAD-CG.2005.50.

Yamamoto, J.K., Kikuda, A.T., Koike, K., Campanha, G.A.C., Leite, C.B.B., Endlen, A., Lopes, S.D., 2015. Determination of volumetric uncertainty for geological bodies detected by boreholes. Meas. J. Int. Meas. Confed. 66, 45–53. http://dx.doi.org/10.1016/j.measurement.2015.01.023.